1 **Introducing the MISR Level 2 Near Real-Time Aerosol Product**

4 Marcin. L. Witek[1], Michael J. Garay[1], David J. Diner[1], Michael A. Bull[1], Felix C. Seidel[1], Abigail

5 M. Nastan[1], and Earl G. Hansen[1]

7 [1]Jet Propulsion Laboratory, California Institute of Technology, 4800 Oak Grove Drive,

8 Pasadena, CA 91109, USA

10 **Abstract**

11 Atmospheric aerosols are an important element of Earth's climate system, and have significant

12 impacts on the environment and on human health. Global aerosol modeling has been

13 increasingly used for operational forecasting and as support to decision making. For example,

14 aerosol analyses and forecasts are routinely used to provide air quality information and alerts in

15 both civilian and military applications. The growing demand for operational aerosol forecasting

16 calls for additional observational data that can be assimilated into models to improve model

17 accuracy and predictive skill. These factors have motivated the development, testing, and

18 release of a new near real-time (NRT) level 2 (L2) aerosol product from the Multi-angle Imaging

19 SpectroRadiometer (MISR) instrument on NASA's Terra platform. The NRT product capitalizes

20 on the unique attributes of the MISR aerosol retrieval approach and product contents, such as

21 reliable aerosol optical depth as well as aerosol microphysical information. Several

22 modifications are described that allow for rapid product generation within a three-hour window

23 following acquisition of the satellite observations. Implications for the product quality and

24 consistency are discussed as compared to the current operational L2 MISR aerosol product.

25 Several ways of implementing additional use-specific retrieval screenings are also highlighted.

1. Introduction

Atmospheric aerosols have for long been recognized to influence the climate, environment, and human health (e.g., IPCC, 2013; Lelieveld et al., 2015; Shindell et al., 2013; Turnock et al., 2020). They also affect satellite remote sensing of important geophysical parameters such as ocean color (e.g., Frouin et al., 2019; Gordon, 1997) or greenhouse gas abundance (Butz et al., 2009; Frankenberg et al., 2012; Houweling et al., 2005). Aerosol particles and their properties have been extensively studied in-situ and remotely: from the ground, in the air, and from space. These observational data vary in spatial and temporal coverage, but usually only offer snapshots of local conditions. Since atmospheric aerosols have a life cycle ranging from hours to days, numerical modeling of their emission, transport, and deposition has filled the coverage gaps and extended our understanding of their global impacts. This has given rise to a number of global aerosol reanalyses (Gelaro et al., 2017; Inness et al., 2013, 2019; Lynch et al., 2016; Rienecker et al., 2011) that provide a long-range, gridded, and internally consistent outlook on aerosol burdens around the world. Furthermore, global aerosol modeling has been increasingly used for operational forecasting (e.g., Xian et al., 2019) and as support to decision making, for example in air quality alerts and in non-civilian applications (Liu et al., 2007).

The growing demand for consistent gridded aerosol products has been driving development and steady improvement of numerical predictions. Still, models suffer from often poorly resolved aerosol emissions and sinks and can be affected by errors in the underlying meteorology. As a result, systematic and sampling-related biases in aerosol fields are often found between model simulations and satellite observations (e.g., Buchard et al., 2015; Colarco et al., 2010; Lamarque et al., 2013; Zhang and Reid, 2009). An effective way to mitigate some of these problems is by assimilating aerosol observations into numerical models (e.g., Bocquet et al., 2015; Fu et al., 2017; Sekiyama et al., 2010; Di Tomaso et al., 2017; Werner et al., 2019; Zhang et al., 2008). Satellite observations of aerosol optical and microphysical properties are inseparable from these data assimilation activities as they offer the necessary data volume, near-global coverage, and frequent repeat cycle. However, an often-considerable latency for generating science-quality "standard" satellite products (8 to 40 hours) renders them unsuitable for operational forecasting. This has led to the development of aerosol products within the time frame required by modeling centers, usually three hours from satellite overpass. A range of near real-time (NRT) products has emerged.

One example of a platform that provides users with NRT satellite products and imagery is NASA's Land, Atmosphere Near real-time Capability for EOS (LANCE) project

63   (https://earthdata.nasa.gov/earth-observation-data/near-real-time). A range of instruments

64   deliver various Level 1 (L1) and Level 2 (L2) data products

65   (https://earthdata.nasa.gov/collaborate/open-data-services-and-software/data-information-

66   policy/data-levels), including radiances, land surface properties, and atmospheric

67   thermodynamics and composition within three hours from satellite observation. NRT aerosol

68   products are currently available from the Moderate Resolution Imaging Spectroradiometer

69   (MODIS), Ozone Monitoring Instrument (OMI), and Visible Infrared Imaging Radiometer Suite

70   (VIIRS). NASA's Multi-angle Imaging SpectroRadiometer (MISR) currently provides NRT

71   radiance and cloud motion vector products. The purpose of this paper is to introduce a new

72   MISR NRT L2 aerosol product.

73   This paper is organized as follows. Section 2 and 3 provide brief descriptions of the

74   MISR instrument and the data processing sequence, respectively. Section 4 first outlines the

75   cloud identification methods employed in the MISR aerosol algorithm and then describes

76   algorithmic modifications introduced in the NRT processing. Adjustments to cloud and retrieval

77   screening parameters and their implications are discussed. The global distributions of the NRT

78   product are analyzed in Section 5. Section 6 provides a summary.

79

80   **2. MISR instrument and aerosol data product**

81

82   The MISR instrument flies aboard the NASA Earth Observing System (EOS) Terra satellite,

83   launched in December 1999 to a sun-synchronous descending polar orbit, at an orbital altitude

84   of 705 km, an orbital period of 99 minutes, and an equatorial crossing time of 10:30 a.m. local

85   time. MISR makes 14.56 orbits per day with a repetition cycle (revisit) of 16 days. The orbit

86   tracks are georeferenced to a fixed set of 233 ground paths. With a cross-track swath of about

87   380 km, total Earth coverage is obtained every 9 days at the equator and every 2 days at high

88   latitudes.

89   MISR contains nine pushbroom cameras with viewing angles at the Earth's surface

90   ranging from 0° (nadir) to +/- 70.5° oriented along the direction of the flight track. A point on the

91   ground is imaged by all nine cameras in approximately 7 minutes. The cameras make

92   observations of reflected solar radiance in four spectral bands, centered at 446 (blue), 558

93   (green), 672 (red), and 866 (near-infrared) nm. The spatial resolution depends on the camera

94   and wavelength. The red band has a full 275 m resolution in all cameras. The other three

95   spectral channels are averaged onboard to a 1.1 km resolution in global-mode operation (Diner

96   et al., 1998), with the exception of the nadir camera which preserves the full 275 m resolution in

97   all spectral channels. See https://misr.jpl.nasa.gov/Mission/ for more details.

98   MISR employs two processing pathways for aerosol retrievals, one for observations over

99   land (Martonchik et al., 2009), and another for dark water (DW) (Kalashnikova et al., 2013),

100   which applies over deep oceans, seas, and lakes. Previous versions of the MISR aerosol

101   product were extensively validated over the years (e.g., Kahn et al., 2010; Kahn and Gaitley,

102   2015; Kalashnikova et al., 2013; Shi et al., 2014; Witek et al., 2013) showing high retrieval

103   quality over land and ocean.

104   The current operational version of the MISR aerosol product, designated as version 23

105   (V23), was released publicly in June 2018. It introduced multiple algorithmic, data product, and

106   data usability improvements (Garay et al., 2020; Witek et al., 2018a, 2018b). V23 provides

107   aerosol information with a spatial resolution of 4.4 km x 4.4 km packaged in NetCDF-4 format.

108   Initial validation efforts showed that V23 retrievals are more accurate than previous versions,

109   with most pronounced improvements in the DW algorithm (Garay et al., 2020). V23 retrievals

110   over oceans were extensively validated by Witek et al. (2019), indicating excellent agreement

111   with ground-based observations. Other V23 Aerosol Optical Depth (AOD) evaluation efforts

112   show similar results (e.g., Choi et al., 2019; Sayer et al., 2020; Si et al., 2020; Sogacheva et al.,

113   2020). A first regional insight into retrieved particle properties from the MISR V23 aerosol

114   product shows that MISR generally captures the distinct spatial and temporal features of aerosol

115   type in East Asia (Tao et al., 2020). Furthermore, V23 has greatly improved the quality of

116   reported AOD uncertainties, which now realistically represent retrieval errors (Sayer et al., 2020;

117   Witek et al., 2019). This is especially relevant as pixel-level retrieval uncertainties are very

118   important for satellite data assimilation, which is being increasingly used in aerosol modeling

119   studies (Lynch et al., 2016; Shi et al., 2011, 2013; Zhang and Reid, 2010). MISR data and

120   related documentation can be obtained from: https://asdc.larc.nasa.gov/project/MISR.

121

122   **3. NRT latency and data description**

123

124   MISR currently provides several L1 and L2 near real-time (NRT) radiance and cloud motion

125   vector products (https://earthdata.nasa.gov/earth-observation-data/near-real-time/download-nrt-

126   data/misr-nrt). All MISR NRT processing is based on Level 0 data downlinked in observational

127   sessions. These session-based files, representing portions of a single MISR orbit, usually cover

128   between 10 to 50 minutes of observations, as compared to the full orbit period of 98.9 minutes.

129   This session-based processing is necessary to allow for the fast product delivery required for

130   NRT applications.

131   The new NRT L2 aerosol product file content, described in Data Product Specification

132   (ref), is equivalent to the standard aerosol product (Garay et al., 2020). The NRT L2 aerosol

133   product file name convention is:

134   MISR_AM1_AS_AEROSOL_T{yyyymmddHHMMSS}_P{ppp}_O{oooooo}_F13_0023.nc, where

135   'yyyy', 'mm', and 'dd' are the year, month, and day, and 'HH', 'MM' and 'SS' are the hour,

136   minute, and seconds, respectively. Furthermore, {ppp} is the three-digit path identifier (between

137   001 and 233) and {oooooo} is the six-digit orbit number. The NRT L2 aerosol product files are

138   available for download within three hours of acquisition at NASA's Atmospheric Science Data

139   Center (ASDC) (https://asdc.larc.nasa.gov/project/MISR).

140   For clarity, it is important to distinguish between the MISR L2 NRT, FIRSTLOOK, and

141   standard aerosol products (see Figure 1). NRT is generated within a three-hour time interval

142   after acquisition and uses the same ancillary inputs as FIRSTLOOK. These include the monthly

143   gridded (1.0 degree) snow/ice mask and surface wind speed from the Terrestrial Atmospheric

144   and Surface Climatology (TASC) database and the seasonal Radiometric Camera-by-camera

145   Threshold Dataset (RCTD) (Diner et al., 1999a). Both NRT and FIRSTLOOK utilize TASC and

146   RCTD datasets from the current month/season in the prior year. The FIRSTLOOK product is

147   generated within two days from acquisition and includes cloud classification parameters

148   obtained from the L1 and L2 cloud products. The standard aerosol product is available after final

149   processing is performed on a seasonal basis and within three months past the end of the

150   season, which results in a 3–6-month latency. The final processing utilizes the most recent

151   snow/ice and wind speed data.
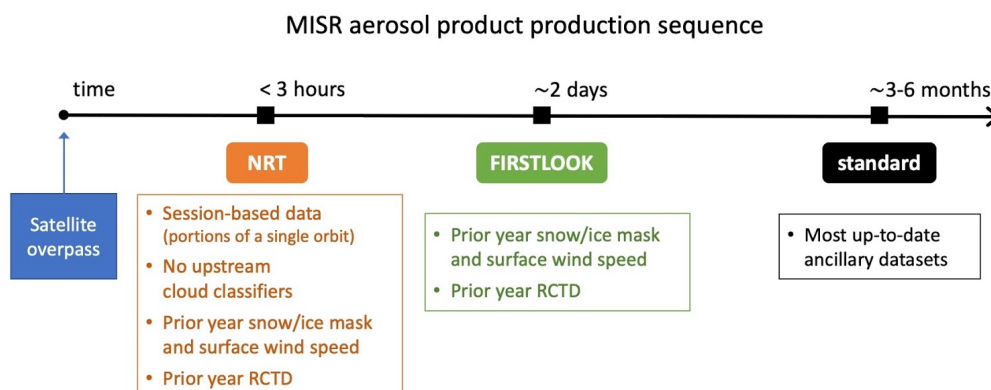
153 Figure 1 *Schematic showing MISR aerosol product delivery timeline. Snow/ice mask and surface wind speed data are monthly*

154 *averages. RCTD stands for Radiometric Camera-by-camera Threshold Dataset. MISR final production (standard product) is*

155 *processed on a seasonal cycle and is often delayed one to three months past the end of each season, which results in up to 6-*

156 *month latency.*

4. NRT aerosol product cloud screening

4.1. Cloud identification

Identification of cloudy pixels is a critical element of all satellite aerosol remote sensing algorithms. MISR employs several cloud identification strategies which can be loosely split into two groups: The first group relies on cloud classifiers previously generated with MISR Level 2 Cloud Detection and Classification algorithm (Diner et al., 1999b), and the second group includes build-in tests that are internal to the aerosol retrieval algorithm (Diner et al., 2008).

4.1.1. Upstream cloud classifiers

The operational MISR aerosol algorithm relies on a range of external input datasets that are either static—for example, a monthly wind speed climatology—or that need to be generated prior to aerosol retrievals in upstream processing. A notable example of such external inputs to the standard and FIRSTLOOK algorithms are cloud classification parameters obtained from the MISR L2 cloud product. An important implication of this dependency is that aerosol processing needs to wait for the cloud product to be generated, creating a time lag that is prohibitive for NRT applications. Typically, the L2 cloud product is generated within about 18 hours of

177   overpass, and the MISR L2 FIRSTLOOK aerosol processing is completed within about 2 days.

178   In order to produce an L2 aerosol product within an about three-hour time frame, the algorithm

179   needs to operate without the upstream cloud classifiers.

180   Two specific L2 cloud classification parameters utilized in aerosol processing are the

181   MISR Stereoscopically-Derived Cloud Mask (SDCM) and the Angular Signature Cloud Mask

182   (ASCM) (Diner et al., 1999b; Girolamo and Davies, 1994). In addition to these L2 products, the

183   Radiometric Camera-by-camera Cloud Mask (RCCM) (Diner et al., 1999a; Girolamo and

184   Davies, 1995) retrieved in L1B processing is also employed. All three parameters are reported

185   at 1.1 km x 1.1 km resolution. It should be noted that RCCM also serves as an input to the

186   algorithm that generates SDCM and ASCM, indicating that these parameters are not

187   independent.

188   In the standard aerosol algorithm, the RCCM, SDCM, and ASCM cloud masks are used

189   together to determine whether a particular 1.1 km x 1.1 km subregion is clear or cloudy. The

190   implication is that if any of the 9 MISR cameras is designated as cloudy in a subregion, this

191   subregion is excluded from aerosol retrieval. The clear/cloudy decision logic depends on the

192   underlying surface type, assigned into three categories: land, water, and snow/ice. Generally, a

193   "clear" outcome is favored over the two most frequently used surface types, land and water,

194   assigning a subregion as cloudy only if the RCCM and SDCM masks indicate a cloud. The logic

195   is considerably more conservative over snow/ice surfaces due to difficulties in distinguishing

196   clouds from the underlying bright features. Details of the cloud mask decision logic over different

197   surface types can be found in Diner et al. (2008).

198   Analyzing three months of V23 L2 aerosol product (March, April, May, 2020) indicates

199   that the cloud masks along with the brightness test (see 4.1.2) lead to screening of about 50%

200   of retrievals. As such, they have the largest impact on identifying and removing pixels where

201   clouds might be present. These masks and decision pathways, however, have their deficiencies

202   and additional checks were put in place to further decrease the frequency of cloud-

203   contaminated aerosol retrievals.

204

205   **4.1.2. Build-in cloud detection methods**

206

207   In addition to the cloud masks retrieved in the L1B processing (RCCM) and from the L2 Cloud

208   Detection and Classification algorithm (SDCM, ASCM), the MISR aerosol retrieval algorithm

209   relies on three internal tests to further identify cloudy pixels that might have escaped earlier

210   detection. These are (1) the *brightness test*, (2) the *angle-to-angle smoothness test*, and (3) the

211 *angle-to-angle correlation test*. Details of these tests can be found in Diner et al. (2008) or Witek

212 et al. (2013), but a short summary is provided here for completeness.

213 The brightness test is employed to identify clouds that lacked sufficient texture to be

214 picked up by SDCM. For each surface type a fixed threshold is adopted on measured

215 bidirectional reflectance factors (BRFs), and when exceeded in all spectral bands for at least

216 one camera, it renders a subregion unsuitable for aerosol retrieval. The thresholds are set to

217 1.0, 0.5, and 0.5 for snow/ice, land, and water surfaces, respectively. The value of 1.0 means

218 that the brightness test is effectively turned off over snow/ice. Furthermore, the brightness test

219 does not override subregions that were identified as clear by RCCM.

220 The angular smoothness test checks for unusually large variations in the measured

221 equivalent reflectances as a function of camera angle, the premise being that in the absence of

222 artifacts or subpixel clouds, the measured radiance should change smoothly from camera to

223 camera. The test is achieved by fitting a polynomial to equivalent reflectances, separately for aft

224 (+nadir) and forward (+nadir) cameras and each spectral band, and checking if the goodness of

225 fit metric (definition in Diner et al., 2008) exceeds a threshold. If in at least one case the test

226 fails, the subregion is eliminated.

227 Finally, the angle-to-angle correlation test also investigates radiance smoothness and

228 correlation between camera angles, which makes it conceptually similar to the angular

229 smoothness test, but instead utilizes high-resolution information form the red spectral band. It

230 uses 4 x 4 arrays of the 275m spatial resolution red band equivalent reflectances in each 1.1 km

231 x 1.1 km subregion. The test then evaluates spatial variability within the 4 x 4 array for each

232 camera and compares it to a variability within a camera-average template. Variances,

233 covariances, and normalized cross-correlations are calculated (see Diner et al., (2008) for

234 details). If the variability within a camera deviates considerably from the average, this camera

235 might have sub-pixel clouds or other contaminants, and as a result the subregion is excluded

236 from aerosol retrievals.

237 In the three months of data analyzed in this study (March, April, May 2020), the relative

238 occurrence of retrieval screening due the above-mentioned internal tests are about 4.0% and

239 0.1% for the correlation and smoothness tests, respectively. These statistics come from

240 analyzing the output field *Aerosol_Retrieval_Screening_Flags* and as such they do not

241 represent the absolute rates of success of each individual test. That is because the tests are

242 performed in a sequential order and if one of them fails, tests that are next in sequence are not

243 performed. For standard aerosol product generation, the order is: upstream cloud mask

244 described in 4.1.1, the brightness test, the correlation test, and the smoothness test. For

245 example, the correlation test is only performed on pixels that already passed the upstream cloud
246 tests as well as the brightness test. Additionally, the brightness test does not have its own flag in
247 the *Aerosol_Retrieval_Screening_Flags* output but is grouped together with the upstream cloud
248 classifiers.
249
250 **4.2. Retrieval screening using regional cloud parameters**
251
252 Methods described in section 4.1 focus on identifying and excluding cloudy 1.1 km x 1.1 km
253 subregions from the aerosol retrieval process. The retrieval region consists of 16 (4 x 4)
254 subregions. These methods are highly effective at removing cloud-contaminated pixels, but
255 since they rely on MISR visible wavelengths they might miss certain cloud signatures more
256 easily detected in the infrared spectrum (e.g., Gao et al., 1993). For example, MODIS routinely
257 uses its reflective and emissive infrared channels to detect optically thin cirrus clouds
258 (Ackerman et al., 2010; Levy et al., 2013). As a result, MISR cloud detection methods
259 occasionally fail, which leads to visible outliers in retrieved AODs (Witek et al., 2018b). For that
260 reason, an additional set of screenings is applied in an effort to eliminate such unusually high
261 AOD retrievals (Garay et al., 2020). Two of these additional methods look at overall cloudiness
262 in the retrieval region (consisting of 4 x 4 subregions) as well as in a larger area consisting of 3
263 x 3 regions (12 x 12 subregions). The Cloud Screening Parameter (CSP) represents the fraction
264 of clear grid cells within a region, whereas Cloud Screening Parameter Neighbor 3x3 (CSP9) is
265 similar to CSP but for the larger area. If CSP is below 0.7 and CSP9 below 0.5, the retrieval is
266 not reported in the final product intended for most users. However, it is still included in the
267 product's AUXILIARY subcategory and annotated with the term "Raw" to indicate that the
268 product has not undergone recommended quality screenings.
269
270 **4.3. Adjusting cloud screening thresholds**
271
272 **4.3.1. Performance of the prototype NRT product**
273
274 This subsection presents results and analysis of prototype NRT aerosol retrievals. These are
275 obtained prior to any threshold and screening adjustments included in the final version of the
276 product. To differentiate between the final and the prototype NRT products, the latter is donated
277 as NRT_{prot}.

278   As mentioned in the previous section, the NRT processing cannot rely on the cloud

279   masks generated in the L1 and L2 cloud products, namely the RCCM, SDCM, and ASCM. This

280   implies that potentially less screening of cloudy subregions would be applied, increasing the

281   probability of cloud contamination in aerosol retrievals. However, some of the burden of cloud

282   identification is picked up by the built-in cloud tests described in section 4.1.2. The frequency of

283   these tests identifying cloudy pixels increases in NRT processing in comparison to standard

284   processing, in large part mitigating the negative consequences resulting from the lack of the

285   upstream cloud masks. This is well evidenced by examining the normalized probability density

286   functions (*pdf*s) of AOD from spring 2020 (Figure 2). The FIRSTLOOK (red) and NRT_{prot} (blue)

287   lines are very similar, indicating that the built-in cloud tests substitute to a significant extent for

288   the missing upstream cloud masks in generating the NRT_{prot} product. The largest difference

289   occurs in the high-AOD range, suggesting that NRT_{prot} has more retrievals in this regime. The

290   black dotted line shows a *pdf* of the NRT_{prot} AOD retrievals that do not have a matching

291   FIRSTLOOK retrieval. This is labeled as "NRT gained" as it represents additional retrievals

292   obtained in *NRT* processing due to the lack of external cloud masks. The "NRT gained" *pdf* is

293   clearly shifted towards higher AODs, confirming that the NRT_{prot} processing tends to retrieve

294   higher AODs in places where FIRSTLOOK is not available.
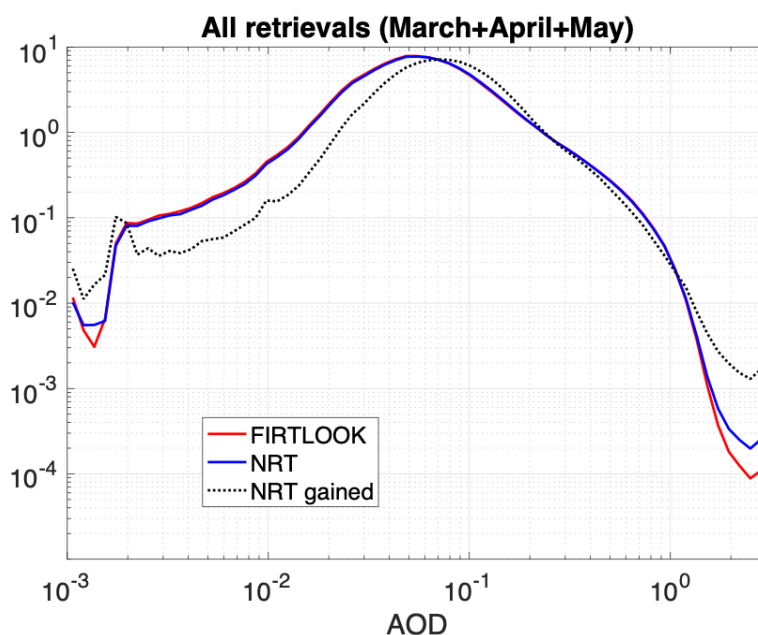
295

296   *Figure 2 AOD normalized probability density functions from FIRSTLOOK, prototype NRT, and prototype NRT retrievals that do not*

297   *have a matching FIRSTLOOK equivalent (labeled as NRT gained). Data statistics are provided in Table 1.*

298   Figure 3 shows *pdf*s of AOD but with retrievals separated between DW (Fig. 3a) and

299   land (Fig. 3b). These *pdf*s indicate that the retrievals over oceans are the main source of

300   increased frequency of high-AODs in the NRT_{prot} product. The *pdf*s over land are virtually

301   unchanged, including a similar distribution of the "NRT gained" retrievals (Fig. 3b). The

302   additional statistics of the data presented in Figs. 2 and 3, including the retrieval count, the

303   mean AOD, and the geometric mean AOD, which is better suited for log-normal distributions of

304   AOD (Sayer et al. 2020), are provided in Table 1.

305   In the 3-month period analyzed in this study (March, April, May, 2020), the NRT_{prot}

306   processing leads to about 6.5% more retrievals than FIRSTLOOK (see Table 1). 5.4 million

307   NRT_{prot} retrievals do not have a matching FIRSTLOOK retrieval (NRT gained), and the majority

308   of them (68%) are DW retrievals. The overall geometric means are almost identical in

309   FIRSTLOOK and NRT_{prot}, although small variations in this statistic are seen in DW and land

310   categories. The NRT gained have visibly higher mean and geometric mean values, the increase

311   coming mainly from DW retrievals. These basic statistics warrant a further look at the NRT_{prot}

312   performance over DW.
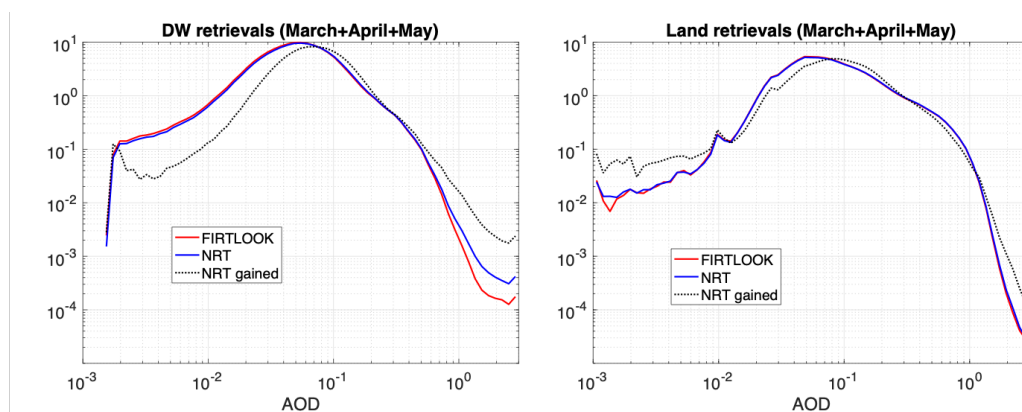
313

314   *Figure 3 Same as in Fig. 2 but with retrievals separated between DW (a) and land (b). Data statistics are provided in Table 1.*

	All retrievals			**DW**			**Land**		
	FL	NRT	NRT gained	FL	NRT	NRT gained	FL	NRT	NRT gained
N (×10⁶)	50.4	53.7	5.4	27.9	31.1	3.7	22.5	22.6	1.7
mean	0.167	0.167	0.172	0.110	0.115	0.146	0.237	0.240	0.228

| geomean | 0.110 | 0.111 | 0.121 | 0.082 | 0.085 | 0.106 | 0.157 | 0.159 | 0.161 |

315 *Table 1 Additional statistics for the data presented in Figs. 2 and 3. FL stand for FIRSTLOOK; NRT gained stands for the prototype*

316 *NRT retrievals that do not have a matching FIRSTLOOK equivalent; geomean stands for the geometric mean AOD.*

317

318 **4.3.2. Sensitivity to CSP and CSP9 thresholds in DW retrievals**

319

320 One way to screen potentially cloud-contaminated high-AOD retrievals is to adjust thresholds on

321 CSP and CSP9 parameters (Garay et al., 2020). This is furthermore justified by the fact that in

322 the absence of RCCM, SDCM, and ASCM in NRT$_{prot}$ processing, less cloudy subregions are

323 identified in a retrieval area and consequently CSP and CSP9 have by default lower values.

324 This argument provides strong justification for investigating sensitivity to increased CSP and

325 CSP9 thresholds in the NRT$_{prot}$ processing.

326   The standard product uses the thresholds of CSP=0.7 and CSP9=0.5 (Garay et al.,

327 2020); when the values of CSP and CSP9 are below these thresholds in a retrieval region, the

328 aerosol retrieval is removed from the data field recommended for users. Figure 4 and Table 2

329 show *pdf*s and AOD statistics for different thresholds of CSP and CSP9 parameters in the

330 NRT$_{prot}$ product over dark water surfaces. There are only minor changes in the *pdf*s when the

331 thresholds are increased, including in the high-AOD regime. The mean and geometric mean

332 decrease gradually but slowly; even at the highest considered thresholds (0.85 for CSP and

333 0.75 for CSP9) these statistics are still above the FIRSTLOOK values. At the same time the

334 number of passing NRT$_{prot}$ retrievals decreases considerably faster, with over 19% of retrievals

335 lost when the highest thresholds are used. These results indicate that adjusting CSP and CSP9

336 thresholds is not an effective strategy to constraining NRT$_{prot}$ retrievals.

337
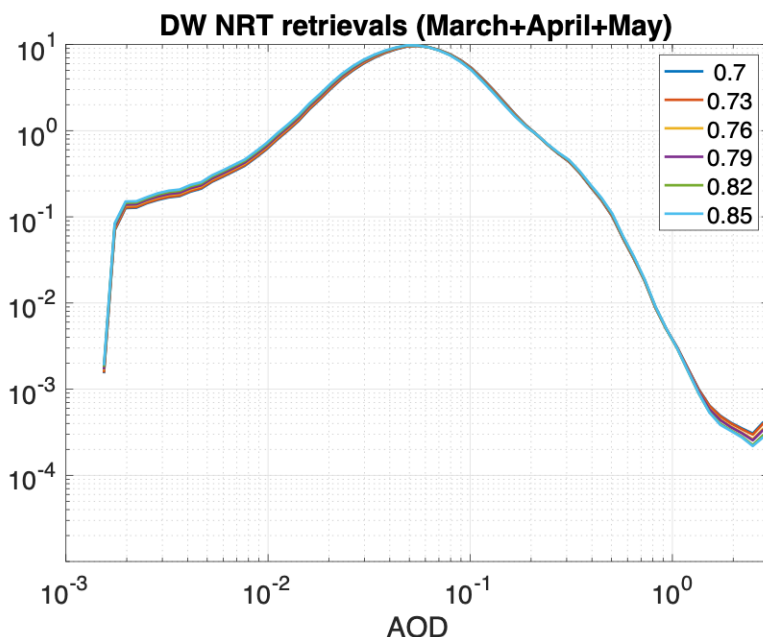
Figure 4 Prototype NRT AOD pdfs over dark water surfaces from spring 2020 obtained with different CSP and CSP9 cloud-

screening thresholds. Data statistics are provided in Table 2.

N (×10^6)	31.1	30.5 (-1.7%)	28.8 (-7.3 %)	28.1 (-9.7%)	26.2 (-15.6%)	25.1 (-19.2%)	FIRSTLOOK 27.9
CSP	≥0.7	≥0.73	≥0.76	≥0.79	≥0.82	≥0.85	
CSP9	≥0.5	≥0.55	≥0.6	≥0.65	≥0.7	≥0.75	
mean	0.1147	0.1145	0.1141	0.114	0.1138	0.1139	0.1105
geomean	0.0848	0.0846	0.0840	0.0837	0.0832	0.0830	0.0824

340

Table 2 Additional statistics for the data presented in Fig. 4. Values for CSP and CSP9 indicate their corresponding thresholds for

341

screening AOD retrievals.

342

343 **4.3.3. Sensitivity to ARCI threshold in DW retrievals**

344

345 V23 of the MISR aerosol product introduced a new parameter, called the aerosol retrieval

346 confidence index (ARCI), that is used to screen high-AOD retrieval outliers caused by cloud

347 contamination and other factors (Witek et al., 2018b). ARCI, defined only for DW retrievals,

348   proved to be an efficient metric at filtering out potentially cloud-contaminated AOD retrievals. In

349   standard processing, retrievals with ARCI < 0.15 are removed from the recommended user

350   field, but are retained in the AUXILIARY group. The 0.15 threshold is well supported through

351   statistical analysis (Witek et al., 2018b), although some erroneous AODs still pass this

352   screening method, suggesting that increasing this threshold might be beneficial in NRT

353   processing.

354   Figure 5 and Table 3 show *pdf*s and AOD statistics for different thresholds of ARCI in the

355   NRT$_{prot}$ product. In this case the differences between ARCI thresholds are quite noticeable,

356   especially in the high-AOD range of retrievals. Increasing the ARCI threshold to 0.2 leads to a

357   loss of about 11% of NRT$_{prot}$ DW retrievals, but the resulting mean and geometric mean are

358   lower than the FIRSTLOOK values. At the same time, the absolute number of NRT$_{prot}$ DW

359   retrievals (27.8 million) is still comparable to the number of FIRSTLOOK DW retrievals (27.9

360   million). The *pdf*s and the statistics suggest that increasing the NRT$_{prot}$ ARCI threshold from

361   0.15 to 0.18 leads to a product that has similar characteristics to FIRSTLOOK.

362
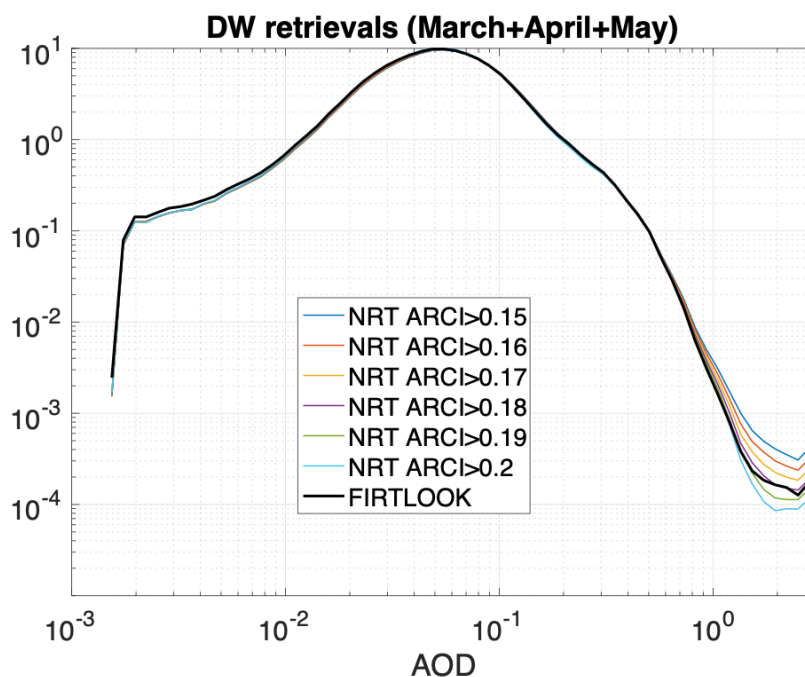
363   *Figure 5 Prototype NRT AOD pdfs from spring 2020 obtained with different ARCI thresholds. Data statistic are provided in Table*

364   *3.*

N (×10⁶)	31.1	30.4 (-2.2%)	29.8 (-4.3%)	29.1 (-6.5%)	28.4 (-8.7%)	27.8 (-10.8%)	Firstlook 27.9
ARCI	≥0.15	≥0.16	≥0.17	≥0.18	≥0.19	≥0.20	
mean	0.1147	0.1133	0.1120	0.1108	0.1096	0.1086	0.1105
geomean	0.0849	0.0841	0.0834	0.0826	0.0819	0.0812	0.0824

365   *Table 3 Additional statistic for the data presented in Fig. 5.*

366

367   **4.3.4. Recommendation for NRT processing**

368

369   The statistical analyses presented in the previous sections indicate that the lack of RCCM,

370   SDCM, and ASCM in NRT processing has negative consequences on the product, especially by

371   allowing more, potentially cloud-contaminated, high-AOD DW retrievals to pass screening

372   criteria. Adjusting build-in cloud screening thresholds on CSP and CSP9 brings only limited

373   benefits at the cost of losing a considerable percentage of retrievals. However, the ARCI

374   threshold adjustments result in much closer statistical correspondence between the NRT$_{prot}$ and

375   FIRSTLOOK AOD retrievals. For that reason, a revised ARCI threshold of 0.18 is implemented

376   in NRT processing. Since the unscreened retrievals are also provided in the AUXILIARY group

377   of the product, users are encouraged to experiment with their own thresholds which might prove

378   more beneficial in specific applications or geographic areas.

379

380   **4.4. Cloud/clear decision logic over snow/ice**

381

382   In section 4.1.1 the impact of upstream cloud classifiers in standard processing—namely the

383   RCCM, SDCM, and ASCM—on the subregion's cloud/clear designation was briefly described.

384   The decision pathway depends on the underlying surface type, which can be either land, water,

385   or snow/ice. Over land and water, the "cloud" outcome is only obtained when both RCCM and

386   SDCM designate the subregion as cloudy. In the absence of RCCM and SDCM the default

387   outcome is "clear". Over snow/ice, however, the logic is more restrictive and favors the "cloudy"

388   designation (Diner et al., 2008). Specifically, when the upstream cloud classifiers are not

389   available, the subregion designation is set to "cloudy" by default. This has important implications

390   on aerosol retrievals in areas where snow and ice occur seasonally.

391   The snow/ice surface mask, unlike land and water, is not static and changes every

392   month. Furthermore, the snow/ice mask input to MISR aerosol processing has a 1.0-degree

393   horizontal resolution, which is re-gridded to a 1.1 km resolution corresponding to the resolution

394   of MISR subregion. In standard processing, FIRSTLOOK retrievals use the snow/ice mask from

395   the same month but in the previous year. The final processing is performed when the current

396   year's monthly snow/ice mask becomes available. The NRT processing, similarly to

397   FIRSTLOOK, relies on the previous year's snow/ice mask. Additionally, given the lack of

398   upstream cloud classifiers, the snow/ice areas are designated as "cloudy" for aerosol retrieval

399   purposes. This is well visualized in Figure 6 which shows the visible image and the

400   corresponding maps of AOD and Aerosol Retrieval Screening Flag in the NRT processing. The

401   dark blue color (index 5) denotes cloudy regions determined using the snow/ice cloud logic. The

402   box-like nature of the excluded areas is associated with the coarse resolution of the snow/ice

403   mask (1.0 degree). The previous year's mask might also not be representative of the current

404   conditions on the ground. It is worth noting that the FIRSTLOOK product often suffers from the

405   same exclusion rules as NRT. This is because of the strict clear/cloud logic over snow/ice

406   surfaces which favors the cloudy outcome; in the case shown in Fig. 6 the AOD gaps in

407   FIRSTLOOK (not shown) look very similar to the NRT product.
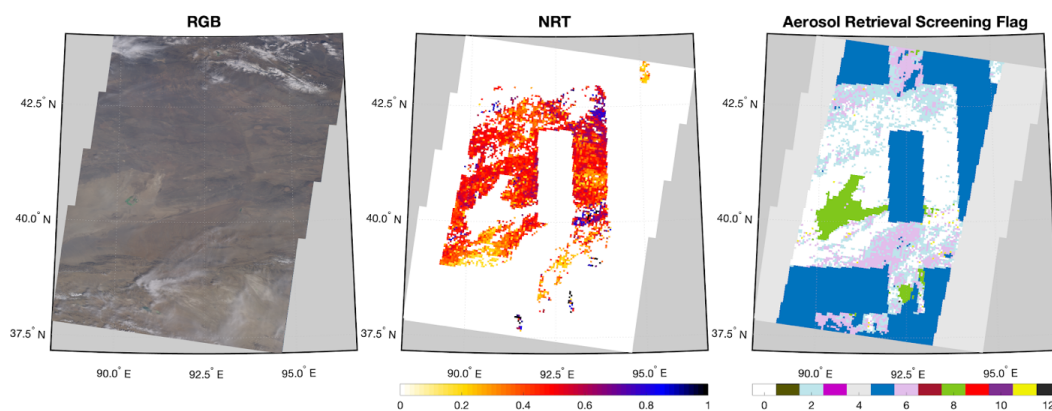
408

409   *Figure 6 Example of snow/ice masking in NRT AOD retrievals. (Left) Visible image of the retrieval area. (Center) Corresponding*

410   *NRT AOD retrievals. (Right) NRT Aerosol Retrieval Screening Flag for the same area; the dark blue color denotes regions*

411   *designated as cloudy.*

412   Several attempts have been made by the MISR science team to improve NRT aerosol

413   retrievals in snow/ice covered areas. However, identifying and isolating snow-covered surfaces

414   in the absence of upstream cloud classifiers proves very challenging. The quality of aerosol

415   retrievals is often negatively affected in such conditions. For that reason, and in an attempt to

416   eliminate as many NRT AOD outliers as possible, the current snow/ice logic is retained in the

417   NRT aerosol processing.

418

419   **5. NRT and FIRSTLOOK differences**

420

421   In this section, geographic distributions of MISR AOD retrievals from FIRSTLOOK and NRT

422   products are analyzed. The datasets encompass three months, March, April, and May of 2020.

423   The NRT AOD retrievals are screened with the revised ARCI threshold of 0.18 as suggested in

424   section 4.3.4. The spatial overlap of the FIRSTLOOK and NRT data is achieved using an

425   intersect of the X_Dim and Y_Dim fields in the two data products.

426   Figure 7 shows the global distributions of geometric mean AOD from the (a)

427   FIRSTLOOK and (b) NRT products. The retrievals are gridded at 2-by-2-degree spatial

428   resolution. Fig. 7c shows the AOD difference between the two products.

429   The largest AOD differences are seen in areas with climatologically high cloud cover,

430   especially over the Southern Ocean. In those regions the FIRSTLOOK AODs are predominantly

431   higher than the NRT AODs. This is due to the increased ARCI threshold in NRT (0.18 vs. 0.15

432   in FIRSTLOOK) which brings in more aggressive screening of cloud-contaminated retrievals

433   (Witek et al., 2018b). At the same time the lack of cloud classifiers in NRT does not adversely

434   affect AOD distributions, which is consistent with the statistical analysis presented in section

435   4.2.3.
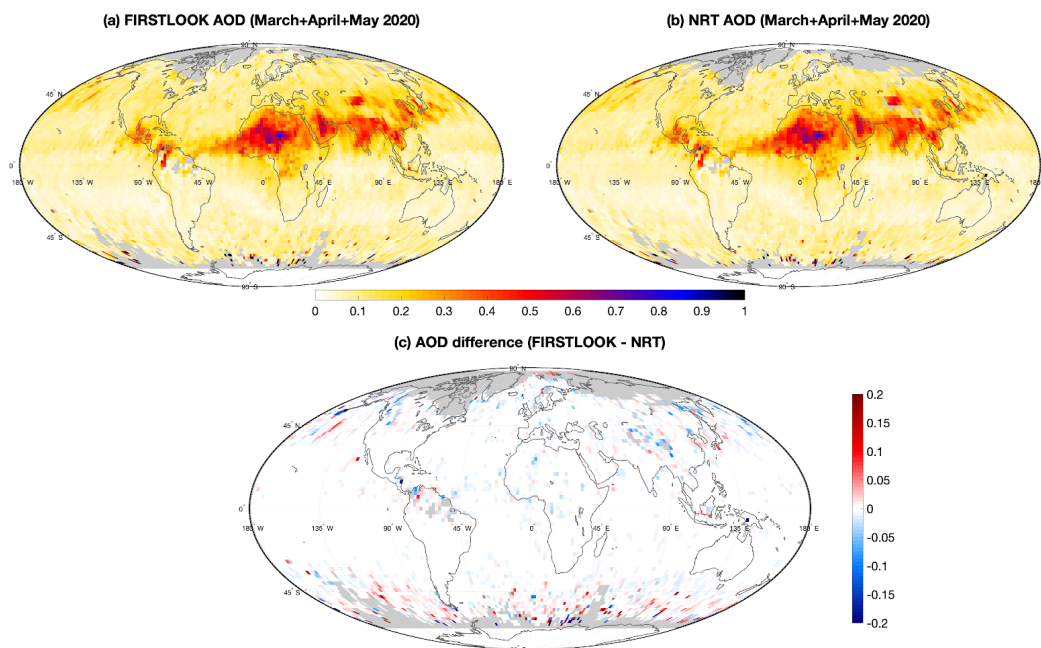
436

437 *Figure 7 (a) Global distribution of FIRSTLOOK AOD geometric mean values across March, April, and May of 2020 on a 2-by-2-*
438 *degree spatial resolution; (b) same as in (a) but for NRT AOD; and (c) AOD difference between FIRSTLOOK and NRT.*

439   Figure 8 complements Fig. 7 by showing (a) the FIRSTLOOK retrieval count distribution

440 as well as (b) the retrieval count difference between the FIRSTLOOK and NRT products.
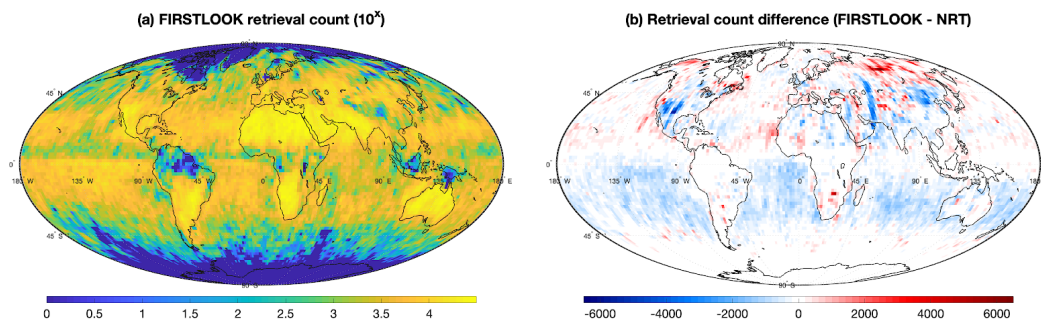
441

442 *Figure 8 (a) Decimal logarithm of the retrieval count from the FIRSTLOOK product in March, April, and May of 2020; (b) retrieval*
443 *count difference between FIRSTLOOK and NRT. Presented values are gridded at 2-by-2-degree spatial resolution*

444   The highest number of retrievals is found over the subtropical continents where the

445 cloud cover is usually the smallest. Over the subtropical oceans in the Southern Hemisphere the

446 NRT retrieval counts are typically lower than in FIRSTLOOK, which is attributed to the increased

447   ARCI threshold in DW retrievals. The lack of hemispheric symmetry in this case is likely due to

448   the seasonal variability (only months in northern spring are analyzed here). The conservative

449   cloud logic over snow/ice surfaces in NRT results in the lower number of retrievals in the high

450   latitudes of the northern hemisphere.

451

452   **6. Summary**

453

454   The MISR V23 aerosol product, publicly available since mid-2018, is a high-resolution state-of-

455   the-art data product from NASA's Terra flagship mission. V23 AOD retrievals have remarkable

456   accuracy compared against ground-based observations (Garay et al., 2020; Tao et al., 2020;

457   Witek et al., 2019) and the product is more intuitive and easier to use than previous versions.

458   The product is available within 2 days from satellite overpass as a FIRSTLOOK version, and

459   within 3-to-6 months as a final science-quality "standard" version that employs the most up-to-

460   date ancillary datasets. In response to the needs of operational user communities, a new MISR

461   L2 NRT aerosol product has been developed with a 3-hour latency.

462   The new NRT algorithm does not depend on the upstream cloud classifiers that are

463   generated in L1 and L2 cloud processing. The lack of cloud classifiers is in large part mitigated

464   by the aerosol algorithm's built-in cloud identification methods. Analysis has shown an

465   increased frequency of high-AOD retrievals, especially over oceans and in climatologically

466   cloudy areas, likely due to an increase in cloud contamination. Adjusting the ARCI threshold in

467   DW retrievals proves highly effective at eliminating some of these high-AOD outliers and

468   improves the NRT product's statistical agreement with the FIRSTLOOK version. The new NRT

469   aerosol product applies an ARCI threshold of 0.18 to mitigate cloud contamination in the

470   absence of upstream cloud masks in NRT processing. The remaining differences in statistical

471   and geographic distributions between NRT and FIRSTLOOK, which includes information from

472   the L2 cloud product, are small and largely confined to areas with high cloud cover.

473   The results of this study also serve as an example of the effects of screening threshold

474   adjustments in MISR aerosol retrievals on AOD statistics and distributions. Researchers

475   interested in particular applications and/or specific geographic regions are encouraged to

476   experiment with their own threshold to achieve most optimal results.

477

478   **Acknowledgements**

479   This research was carried out at the Jet Propulsion Laboratory, California Institute of

480   Technology, under a contract with the National Aeronautics and Space Administration. Support

481   from the MISR project is acknowledged. All data analyzed in this study are publicly available,

482   although the transient nature of FIRSTLOOK and NRT products might limit their availability. The

483   data can be downloaded from https://l0dup05.larc.nasa.gov/cgi-bin/MISR/main.cgi.

484

485

References:

Ackerman, S., Richard, F., Kathleen, S., Yinghui, L., Liam, G., Bryan, B. and Paul, M.: Discriminating clear-sky from cloud with MODIS algorithm theoretical basis document (MOD35), Univ. Wisconsin - Madison, 6th Edn.(October), 129 [online] Available from: http://citeseerx.ist.psu.edu/viewdoc/summary?doi=10.1.1.385.4885, 2010.

Bocquet, M., Elbern, H., Eskes, H., Hirtl, M., Aabkar, R., Carmichael, G. R., Flemming, J., Inness, A., Pagowski, M., Pérez Camaño, J. L., Saide, P. E., San Jose, R., Sofiev, M., Vira, J., Baklanov, A., Carnevale, C., Grell, G. and Seigneur, C.: Data assimilation in atmospheric chemistry models: Current status and future prospects for coupled chemistry meteorology models, Atmos. Chem. Phys., 15(10), 5325–5358, doi:10.5194/acp-15-5325-2015, 2015.

Buchard, V., Da Silva, A. M., Colarco, P. R., Darmenov, A., Randles, C. A., Govindaraju, R., Torres, O., Campbell, J. and Spurr, R.: Using the OMI aerosol index and absorption aerosol optical depth to evaluate the NASA MERRA Aerosol Reanalysis, Atmos. Chem. Phys., 15(10), 5743–5760, doi:10.5194/acp-15-5743-2015, 2015.

Butz, A., Hasekamp, O. P., Frankenberg, C. and Aben, U.: Retrievals of atmospheric CO2 from simulated space-borne measurements of backscattered near-infrared sunlight: Accounting for aerosol effects, Appl. Opt., 48, 3322–3336, doi:10.1364/AO.48.003322, 2009.

Choi, M., Lim, H., Kim, J., Lee, S., Eck, T. F., Holben, B. N., Garay, M. J., Hyer, E. J., Saide, P. E. and Liu, H.: Validation, comparison, and integration of GOCI, AHI, MODIS, MISR, and VIIRS aerosol optical depth over East Asia during the 2016 KORUS-AQ campaign, Atmos. Meas. Tech., 12(8), 4619–4641, doi:10.5194/amt-12-4619-2019, 2019.

Colarco, P., Da Silva, A., Chin, M. and Diehl, T.: Online simulations of global aerosol distributions in the NASA GEOS-4 model and comparisons to satellite and ground-based aerosol optical depth, J. Geophys. Res. Atmos., 115(14), doi:10.1029/2009JD012820, 2010.

Diner, D. J., Beckert, J. C., Reilly, T. H., Bruegge, C. J., Conel, J. E., Kahn, R. A., Martonchik, J. V., Ackerman, T. P., Davies, R., Gerstl, S. A. W., Gordon, H. R., Muller, J. P., Myneni, R. B., Sellers, P. J., Pinty, B. and Verstraete, M. M.: Multiangle Image Spectroradiometer (MISR)

513   instrument description and experiment overview, IEEE Trans. Geosci. Remote Sens., 36(4),

514   1072–1087, 1998.

515   Diner, D. J., Di Girolamo, L. and Clothiaux, E. E.: Level 1 Cloud Detection Algorithm

516   Theoretical Basis, Jet Propuls. Lab. Calif. Inst. Technol., D-13397(Rev. B), 1999a.

517   Diner, D. J., Davies, R., Di Girolamo, L., Horvath, A., Moroney, C., Muller, J. P., Paradise, S.

518   R., Wenkert, D. and Zong, J.: Level 2 Cloud Detection and Classification Algorithm Theoretical

519   Basis, Jet Propuls. Lab. Calif. Inst. Technol., D-11399(Rev. D), 1999b.

520   Diner, D. J., Abdou, W. A., Ackerman, T. P., Crean, K., Gordon, H. R., Kahn, R. A.,

521   Martonchik, J. V, McMuldroch, S., Paradise, S. R. and Pinty, B.: Level 2 aerosol retrieval

522   algorithm theoretical basis, Jet Propuls. Lab. Calif. Inst. Technol., D-11400(Rev. G), 2008.

523   Frankenberg, C., Hasekamp, O., O'Dell, C., Sanghavi, S., Butz, A. and Worden, J.: Aerosol

524   information content analysis of multi-angle high spectral resolution measurements and its benefit

525   for high accuracy greenhouse gas retrievals, Atmos. Meas. Tech., 5(7), 1809–1821,

526   doi:10.5194/amt-5-1809-2012, 2012.

527   Frouin, R. J., Franz, B. A., Ibrahim, A., Knobelspiesse, K., Ahmad, Z., Cairns, B., Chowdhary,

528   J., Dierssen, H. M., Tan, J., Dubovik, O., Huang, X., Davis, A. B., Kalashnikova, O., Thompson,

529   D. R., Remer, L. A., Boss, E., Coddington, O., Deschamps, P. Y., Gao, B. C., Gross, L.,

530   Hasekamp, O., Omar, A., Pelletier, B., Ramon, D., Steinmetz, F. and Zhai, P. W.: Atmospheric

531   Correction of Satellite Ocean-Color Imagery During the PACE Era, Front. Earth Sci., 7,

532   doi:10.3389/feart.2019.00145, 2019.

533   Fu, G., Prata, F., Xiang Lin, H., Heemink, A., Segers, A. and Lu, S.: Data assimilation for

534   volcanic ash plumes using a satellite observational operator: A case study on the 2010

535   Eyjafjallajökull volcanic eruption, Atmos. Chem. Phys., 17(2), 1187–1205, doi:10.5194/acp-17-

536   1187-2017, 2017.

537   Gao, B. C., Goetz, A. F. H. and Wiscombe, W. J.: Cirrus cloud detection from Airborne Imaging

538   Spectrometer data using the 1.38 µm water vapor band, Geophys. Res. Lett., 20(3), 301–304,

539   doi:10.1029/93GL00106, 1993.

540 Garay, M. J., Witek, M. L., Kahn, R. A., Seidel, F. C., Limbacher, J. A., Bull, M. A., Diner, D.
541 J., Hansen, E. G. E. G., Kalashnikova, O. V., Lee, H., Nastan, A. M. and Yu, Y.: Introducing the
542 4.4km spatial resolution Multi-Angle Imaging SpectroRadiometer (MISR) aerosol product,
543 Atmos. Meas. Tech., 13(2), 593–628, doi:10.5194/amt-13-593-2020, 2020.

544 Gelaro, R., McCarty, W., Suárez, M. J., Todling, R., Molod, A., Takacs, L., Randles, C. A.,
545 Darmenov, A., Bosilovich, M. G., Reichle, R., Wargan, K., Coy, L., Cullather, R., Draper, C.,
546 Akella, S., Buchard, V., Conaty, A., da Silva, A. M., Gu, W., Kim, G. K., Koster, R., Lucchesi,
547 R., Merkova, D., Nielsen, J. E., Partyka, G., Pawson, S., Putman, W., Rienecker, M., Schubert,
548 S. D., Sienkiewicz, M. and Zhao, B.: The modern-era retrospective analysis for research and
549 applications, version 2 (MERRA-2), J. Clim., 30(14), 5419–5454, doi:10.1175/JCLI-D-16-
550 0758.1, 2017.

551 Girolamo, L. Di and Davies, R.: A Band-Differenced Angular Signature Technique for Cirrus
552 Cloud Detection, IEEE Trans. Geosci. Remote Sens., 32(4), 890–896, doi:10.1109/36.298017,
553 1994.

554 Girolamo, L. Di and Davies, R.: The Image Navigation Cloud Mask for the Multiangle Imaging
555 Spectroradiometer (MISR), J. Atmos. Ocean. Technol., 12(6), doi:10.1175/1520-
556 0426(1995)012<1215:tincmf>2.0.co;2, 1995.

557 Gordon, R.: Atmospheric correction of ocean color imagery in the Earth Observing System era,
558 J. Geophys. Res. - Atmos., 102(D14), 17081–17106, doi:10.1029/96JD02443, 1997.

559 Houweling, S., Hartmann, W., Aben, I., Schrijver, H., Skidmore, J., Roelofs, G. J. and Breon, F.
560 M.: Evidence of systematic errors in SCIAMACHY-observed CO2 due to aerosols, Atmos.
561 Chem. Phys., 5(11), 3003–3013, doi:10.5194/acp-5-3003-2005, 2005.

562 Inness, A., Baier, F., Benedetti, A., Bouarar, I., Chabrillat, S., Clark, H., Clerbaux, C., Coheur,
563 P., Engelen, R. J., Errera, Q., Flemming, J., George, M., Granier, C., Hadji-Lazaro, J., Huijnen,
564 V., Hurtmans, D., Jones, L., Kaiser, J. W., Kapsomenakis, J., Lefever, K., Leitão, J., Razinger,
565 M., Richter, A., Schultz, M. G., Simmons, A. J., Suttie, M., Stein, O., Thépaut, J. N., Thouret,
566 V., Vrekoussis, M. and Zerefos, C.: The MACC reanalysis: An 8 yr data set of atmospheric
567 composition, Atmos. Chem. Phys., 13(8), 4073–4109, doi:10.5194/acp-13-4073-2013, 2013.

568 Inness, A., Ades, M., Agustí-Panareda, A., Barré, J., Benedictow, A., Blechschmidt, A.-M.,

569 Dominguez, J. J., Engelen, R., Eskes, H., Flemming, J., Huijnen, V., Jones, L., Kipling, Z.,

570 Massart, S., Parrington, M., Peuch, V.-H., Razinger, M., Remy, S., Schulz, M. and Suttie, M.:

571 The CAMS reanalysis of atmospheric composition, Atmos. Chem. Phys., 19(6), 3515–3556,

572 doi:10.5194/acp-19-3515-2019, 2019.

573 IPCC: Climate Change 2013: The Physical Science Basis. Contribution of Working Group I to

574 the Fifth Assessment Report of the Intergovernmental Panel on Climate Change, edited by T. F.

575 Stocker, D. Qin, G. K. Plattner, M. M. B. Tignor, S. K. Allen, J. Boschung, A. Nauels, Y. Xia,

576 V. Bex, and P. M. Midgley, Cambridge University Press, Cambridge, United Kingdom and New

577 York, NY, USA., 2013.

578 Kahn, R. A. and Gaitley, B. J.: An analysis of global aerosol type as retrieved by MISR, J.

579 Geophys. Res. Atmos., 120(9), 4248–4281, doi:10.1002/2015JD023322, 2015.

580 Kahn, R. A., Gaitley, B. J., Garay, M. J., Diner, D. J., Eck, T. F., Smirnov, A. and Holben, B. N.:

581 Multiangle Imaging SpectroRadiometer global aerosol product assessment by comparison with

582 the Aerosol Robotic Network, J. Geophys. Res. Atmos., 115(23), doi:10.1029/2010JD014601,

583 2010.

584 Kalashnikova, O. V., Garay, M. J., Martonchik, J. V. and Diner, D. J.: MISR Dark Water aerosol

585 retrievals: Operational algorithm sensitivity to particle non-sphericity, Atmos. Meas. Tech., 6(8),

586 2131–2154, doi:10.5194/amt-6-2131-2013, 2013.

587 Lamarque, J. F., Shindell, D. T., Josse, B., Young, P. J., Cionni, I., Eyring, V., Bergmann, D.,

588 Cameron-Smith, P., Collins, W. J., Doherty, R., Dalsoren, S., Faluvegi, G., Folberth, G., Ghan,

589 S. J., Horowitz, L. W., Lee, Y. H., MacKenzie, I. A., Nagashima, T., Naik, V., Plummer, D.,

590 Righi, M., Rumbold, S. T., Schulz, M., Skeie, R. B., Stevenson, D. S., Strode, S., Sudo, K.,

591 Szopa, S., Voulgarakis, A. and Zeng, G.: The atmospheric chemistry and climate model

592 intercomparison Project (ACCMIP): Overview and description of models, simulations and

593 climate diagnostics, Geosci. Model Dev., 6(1), 179–206, doi:10.5194/gmd-6-179-2013, 2013.

594 Lelieveld, J., Evans, J. S., Fnais, M., Giannadaki, D. and Pozzer, A.: The contribution of outdoor

595 air pollution sources to premature mortality on a global scale, Nature, 525(7569), 367–371,

596 doi:10.1038/nature15371, 2015.

597 Levy, R. C., Mattoo, S., Munchak, L. A., Remer, L. A., Sayer, A. M., Patadia, F. and Hsu, N. C.:
598 The Collection 6 MODIS aerosol products over land and ocean, Atmos. Meas. Tech., 6(11),
599 2989–3034, doi:10.5194/amt-6-2989-2013, 2013.

600 Liu, M., Westphal, D. L., Walker, A. L., Holt, T. R., Richardson, K. A. and Miller, S. D.:
601 COAMPS real-time dust storm forecasting during operation Iraqi freedom, Weather Forecast.,
602 22(1), 192–206, doi:10.1175/WAF971.1, 2007.

603 Lynch, P., Reid, J. S., Westphal, D. L., Zhang, J., Hogan, T. F., Hyer, E. J., Curtis, C. A., Hegg,
604 D. A., Shi, Y., Campbell, J. R., Rubin, J. I., Sessions, W. R., Turk, F. J. and Walker, A. L.: An
605 11-year global gridded aerosol optical thickness reanalysis (v1.0) for atmospheric and climate
606 sciences, Geosci. Model Dev., 9(4), 1489–1522, doi:10.5194/gmd-9-1489-2016, 2016.

607 Martonchik, J. V., Kahn, R. A. and Diner, D. J.: Retrieval of aerosol properties over land using
608 MISR observations, in Satellite Aerosol Remote Sensing over Land, pp. 267–293, Springer
609 Berlin Heidelberg., 2009.

610 Rienecker, M. M., Suarez, M. J., Gelaro, R., Todling, R., Bacmeister, J., Liu, E., Bosilovich, M.
611 G., Schubert, S. D., Takacs, L., Kim, G. K., Bloom, S., Chen, J., Collins, D., Conaty, A., Da
612 Silva, A., Gu, W., Joiner, J., Koster, R. D., Lucchesi, R., Molod, A., Owens, T., Pawson, S.,
613 Pegion, P., Redder, C. R., Reichle, R., Robertson, F. R., Ruddick, A. G., Sienkiewicz, M. and
614 Woollen, J.: MERRA: NASA's modern-era retrospective analysis for research and applications,
615 J. Clim., 24, 3624–3648, doi:10.1175/JCLI-D-11-00015.1, 2011.

616 Sayer, A. M., Govaerts, Y., Kolmonen, P., Lipponen, A., Luffarelli, M., Mielonen, T., Patadia,
617 F., Popp, T., Povey, A. C., Stebel, K. and Witek, M. L.: A review and framework for the
618 evaluation of pixel-level uncertainty estimates in satellite aerosol remote sensing, Atmos. Meas.
619 Tech., 13(2), 373–404, doi:10.5194/amt-13-373-2020, 2020.

620 Sekiyama, T. T., Tanaka, T. Y., Shimizu, A. and Miyoshi, T.: Data assimilation of CALIPSO
621 aerosol observations, Atmos. Chem. Phys., 10(1), 39–49, doi:10.5194/acp-10-39-2010, 2010.

622 Shi, Y., Zhang, J., Reid, J. S., Holben, B., Hyer, E. J. and Curtis, C.: An analysis of the collection

623   5 MODIS over-ocean aerosol optical depth product for its implication in aerosol assimilation,

624   Atmos. Chem. Phys., 11(2), 557–565, doi:10.5194/acp-11-557-2011, 2011.

625   Shi, Y., Zhang, J., Reid, J. S., Hyer, E. J. and Hsu, N. C.: Critical evaluation of the MODIS Deep

626   Blue aerosol optical depth product for data assimilation over North Africa, Atmos. Meas. Tech.,

627   6(4), 949–969, doi:10.5194/amt-6-949-2013, 2013.

628   Shi, Y., Zhang, J., Reid, J. S., Liu, B. and Hyer, E. J.: Critical evaluation of cloud contamination

629   in the MISR aerosol products using MODIS cloud mask products, Atmos. Meas. Tech., 7(6),

630   1791–1801, doi:10.5194/amt-7-1791-2014, 2014.

631   Shindell, D. T., Lamarque, J. F., Schulz, M., Flanner, M., Jiao, C., Chin, M., Young, P. J., Lee,

632   Y. H., Rotstayn, L., Mahowald, N., Milly, G., Faluvegi, G., Balkanski, Y., Collins, W. J.,

633   Conley, A. J., Dalsoren, S., Easter, R., Ghan, S., Horowitz, L., Liu, X., Myhre, G., Nagashima,

634   T., Naik, V., Rumbold, S. T., Skeie, R., Sudo, K., Szopa, S., Takemura, T., Voulgarakis, A.,

635   Yoon, J. H. and Lo, F.: Radiative forcing in the ACCMIP historical and future climate

636   simulations, Atmos. Chem. Phys., 13(6), 2939–2974, doi:10.5194/acp-13-2939-2013, 2013.

637   Si, Y., Chen, L., Xiong, X., Shi, S., Husi, L. and Cai, K.: Evaluation of the MISR fine resolution

638   aerosol product using MODIS, MISR, and ground observations over China, Atmos. Environ.,

639   223(December 2019), 117229, doi:10.1016/j.atmosenv.2019.117229, 2020.

640   Sogacheva, L., Popp, T., Sayer, A. M., Dubovik, O., Garay, M. J., Heckel, A., Hsu, N. C.,

641   Jethva, H., Kahn, R. A., Kolmonen, P., Kosmale, M., de Leeuw, G., Levy, R. C., Litvinov, P.,

642   Lyapustin, A., North, P., Torres, O. and Arola, A.: Merging regional and global aerosol optical

643   depth records from major available satellite products, Atmos. Chem. Phys., 20(4), 2031–2056,

644   doi:10.5194/acp-20-2031-2020, 2020.

645   Tao, M., Wang, J., Li, R., Chen, L., Xu, X., Wang, L., Tao, J., Wang, Z. and Xiang, J.:

646   Characterization of Aerosol Type Over East Asia by 4.4 km MISR Product: First Insight and

647   General Performance, J. Geophys. Res. Atmos., 125(13), 1–16, doi:10.1029/2019JD031909,

648   2020.

649   Di Tomaso, E., Schutgens, N. A. J., Jorba, O. and García-Pando, C. P.: Assimilation of MODIS

650   Dark Target and Deep Blue observations in the dust aerosol component of NMMB-MONARCH

651   version 1.0, Geosci. Model Dev., 10(3), 1107–1129, doi:10.5194/gmd-10-1107-2017, 2017.

652   Turnock, S. T., Allen, R. J., Andrews, M., Bauer, S. E., Deushi, M., Emmons, L., Good, P.,

653   Horowitz, L., John, J. G., Michou, M., Nabat, P., Naik, V., Neubauer, D., O'Connor, F. M.,

654   Olivié, D., Oshima, N., Schulz, M., Sellar, A., Shim, S., Takemura, T., Tilmes, S., Tsigaridis, K.,

655   Wu, T. and Zhang, J.: Historical and future changes in air pollutants from CMIP6 models,

656   Atmos. Chem. Phys., 20(23), 14547–14579, doi:10.5194/acp-20-14547-2020, 2020.

657   Werner, M., Kryza, M. and Guzikowski, J.: Can data assimilation of surface PM2.5 and Satellite

658   AOD improve WRF-Chem Forecasting? A case study for two scenarios of particulate air

659   pollution episodes in Poland, Remote Sens., 11(20), doi:10.3390/rs11202364, 2019.

660   Witek, M. L., Garay, M. J., Diner, D. J. and Smirnov, A.: Aerosol optical depths over oceans: A

661   view from MISR retrievals and collocated MAN and AERONET in situ observations, J.

662   Geophys. Res. Atmos., 118(22), 12620–12633, doi:10.1002/2013JD020393, 2013.

663   Witek, M. L., Diner, D. J., Garay, M. J., Xu, F., Bull, M. A. and Seidel, F. C.: Improving MISR

664   AOD Retrievals with Low-Light-Level Corrections for Veiling Light, IEEE Trans. Geosci.

665   Remote Sens., 56(3), 1251–1268, doi:10.1109/TGRS.2017.2727342, 2018a.

666   Witek, M. L., Garay, M. J., Diner, D. J., Bull, M. A. and Seidel, F. C.: New approach to the

667   retrieval of AOD and its uncertainty from MISR observations over dark water, Atmos. Meas.

668   Tech., 11(1), 429–439, doi:10.5194/amt-11-429-2018, 2018b.

669   Witek, M. L., Garay, M. J., Diner, D. J. and Smirnov, A.: Oceanic Aerosol Loading Derived

670   From MISR's 4.4 km (V23) Aerosol Product, J. Geophys. Res. Atmos., 124(17–18), 10154–

671   10174, doi:10.1029/2019JD031065, 2019.

672   Xian, P., Reid, J. S., Hyer, E. J., Sampson, C. R., Rubin, J. I., Ades, M., Asencio, N., Basart, S.,

673   Benedetti, A., Bhattacharjee, P. S., Brooks, M. E., Colarco, P. R., da Silva, A. M., Eck, T. F.,

674   Guth, J., Jorba, O., Kouznetsov, R., Kipling, Z., Sofiev, M., Perez Garcia-Pando, C., Pradhan,

675   Y., Tanaka, T., Wang, J., Westphal, D. L., Yumimoto, K. and Zhang, J.: Current state of the

676   global operational aerosol multi-model ensemble: An update from the International Cooperative

677   for Aerosol Prediction (ICAP), Q. J. R. Meteorol. Soc., 145, 176–209, doi:10.1002/qj.3497,

678   2019.

679   Zhang, J. and Reid, J. S.: An analysis of clear sky and contextual biases using an operational

680   over ocean MODIS aerosol product, Geophys. Res. Lett., 36(15), doi:10.1029/2009GL038723,

681   2009.

682   Zhang, J. and Reid, J. S.: A decadal regional and global trend analysis of the aerosol optical

683   depth using a data-assimilation grade over-water MODIS and Level 2 MISR aerosol products,

684   Atmos. Chem. Phys., 10(22), 10949–10963, doi:10.5194/acp-10-10949-2010, 2010.

685   Zhang, J., Reid, J. S., Westphal, D. L., Baker, N. L. and Hyer, E. J.: A system for operational

686   aerosol optical depth data assimilation over global oceans, J. Geophys. Res. Atmos., 113(10), 1–

687   13, doi:10.1029/2007JD009065, 2008.

688